applied sciences

MDPI

Article

Parametric Analysis of Static–Dynamic Characteristics of Adjacent Tunnels in Super-Large Twin Tunnels by DEM

Lin Wu [1], Zhuoyuan Cao [1], Xiaoya Bian [1,*], Jiayan Wang [1] and Hong Guo [2]

[1] School of Civil Engineering and Architecture, Wuhan Institute of Technology, Wuhan 430074, China; wulin_civil@wit.edu.cn (L.W.); czy2301944835@163.com (Z.C.); wjy1972451295@163.com (J.W.)
[2] School of Civil Engineering and Architecture, Shaanxi University of Technology, Hanzhong 723001, China; hguo@snut.edu.cn
* Correspondence: wit_bianxy@hust.edu.cn; Tel.: +86-136-5980-5277

Featured Application

The parametric analysis of super-large-diameter twin tunnels under train-induced vibrations provides scientific guidance for the design, construction, and operation of super-large twin tunnel engineering.

Abstract

The dynamic characteristics of super-large-diameter twin tunnels under train vibration loads have become a critical issue affecting not only the engineering safety of their own tunnels but also adjacent tunnels. A numerical model of super-large-diameter (D = 15.2 m) twin tunnels was established by the discrete element method (DEM) to analyze the static and dynamic responses of adjacent tunnel structures and surroundings under train-induced vibrations. Three parameters were considered: internal walls, absolute and relative spacing, and water pressure. The results indicate that internal walls in super-large twin tunnels can significantly reduce the static and dynamic responses in both the structures and surroundings of the adjacent tunnel. The vehicular lane board (wall2) plays a determinative role, followed by the smoke exhaust board (wall1), while the left and right partition walls (wall3 and wall4) exhibit the least effectiveness. The static–dynamic responses of the liners and surroundings of adjacent tunnels in super-large twin tunnels are significantly greater than those in smaller twin tunnels when the absolute spacing is identical. Moreover, the significant differences in displacement and velocity between the liners and surroundings can lead to cracks, leakage, or even instability. Appropriate water pressure (149 kPa) can effectively mitigate dynamic responses in adjacent tunnel structures and surroundings. The dynamic characteristics of super-large-diameter twin tunnels differ markedly from those of small-diameter twin tunnels, with internal walls, twin tunnel spacing, and water pressure all influencing their static and dynamic behaviors. This study provides theoretical guidance for the design and operation of super-large-diameter twin tunnels.

Keywords: super-large tunnel; twin tunnels; train vibration load; static–dynamic characteristics; discrete element method (DEM)

check for updates

Academic Editor: Valentino Paolo Berardi

Received: 30 April 2025
Revised: 12 June 2025
Accepted: 21 June 2025
Published: 25 June 2025

Citation: Wu, L.; Cao, Z.; Bian, X.; Wang, J.; Guo, H. Parametric Analysis of Static–Dynamic Characteristics of Adjacent Tunnels in Super-Large Twin Tunnels by DEM. *Appl. Sci.* **2025**, *15*, 7124. https://doi.org/10.3390/app15137124

Copyright: © 2025 by the authors. Licensee MDPI, Basel, Switzerland. This article is an open access article distributed under the terms and conditions of the Creative Commons Attribution (CC BY) license (https://creativecommons.org/licenses/by/4.0/).

1. Introduction

With the rapid development of urban rail transit, super-large-diameter twin tunnels designed for combined highway and railway use are being extensively constructed due to their advantages in conserving underground space [1,2]. Subway train operations cause

vibrations in their own and adjacent tunnel structures and surrounding soil, impacting stability, durability, and the safety and comfort of adjacent tunnels. As a result, research on the dynamic behavior of super-large-diameter twin tunnels is gaining more attention.

For small-diameter tunnels (d = 6.0–6.2 m), Heidary et al. [3] found ground vibration increases with higher axle loads when two trains pass in opposite directions inside twin tunnels (d = 6.0 m). Zhou et al. [4] conducted a 50× g centrifuge test on parallel tunnels (d = 6.0 m) under train and sweeping frequency loads. Their results showed that twin-tunnel interaction significantly amplifies dynamic responses. Li et al. [5] found the influence range of shield driving, and the interaction between the twin tunnels (d = 6.2 m) with different axis spacings in shield driving. Pang et al. [6] established a robust methodological framework for assessing tunnel face stability and offers valuable guidance for the design and construction of shield tunnels (d = 6.0 m) in analogous geological and operational contexts. Li et al. [7] demonstrated that the calculated displacement settlement trends align closely with the numerical simulation and are consistent with field monitoring data when new tunnels (d = 6.2 m) are excavated above existing tunnels. These studies demonstrate that research on standard-diameter tunnels (d = 6.0–6.2 m) under train-induced vibrations has been relatively thorough.

In research on large-diameter tunnels (D = 10.0–15.0 m), Wang et al. [8] found that wider faults significantly increase plastic zone expansion in the lining of a fault-crossing tunnel (D = 10 m). Liu et al. [9] demonstrated that shield speed directly affects subgrade settlement, informing construction parameter optimization in sensitive areas in twin shield tunnels (D = 12.8 m). Zhang et al. [10] conducted long-term monitoring of segment loads and structural internal forces in a large-diameter shield tunnel (D = 14.5 m) and found that actual earth pressures are just 48–60% of theoretical values, which provides an empirical basis for the load calculation of large-diameter tunnels. These studies collectively demonstrate that large-diameter tunnels exhibit distinct dynamic characteristics compared to conventional sizes, warranting further investigation.

In research on super-large-diameter tunnels ($D \geq$ 15.0 m) [11–14], Shi et al. [15] defined the longitudinal ground settlement patterns of twin tunnels (D = 15 m), combining the three-dimensional random finite element methods and Monte Carlo simulation. Kou et al. [16] provided critical design guidelines of large-diameter tunnel (D = 15 m) joints for high-pressure environments. Wu et al. [17] compared vibration characteristics between super-large (D = 15.2 m) and small (d = 6.2 m) river-crossing twin tunnels using DEM models, demonstrating larger tunnels' superior stability when the relative spacing is the same (l/d = 0.25, l/D = 0.25). Wang et al. [18] proved that thicker secondary linings enhance load capacity by optimizing segment-lining interaction in 15.2 m shield tunnels. Guo et al. [19] found that internal structures effectively reduce dynamic responses by physical model tests (D = 15.2 m). Li et al. [20] studied the impact of 15.4 m shield tunnel construction on adjacent existing subway tunnels by finite element model, measuring 17.9 mm displacements in adjacent subway tunnels and evaluating isolation pile effectiveness. Xue et al. [21] revealed that excavation of super-large-diameter tunnels (D = 15.56 m) causes the maximum compressive stress in the existing tunnel lining at the haunch and the maximum tensile stress at the crown. From the above research results, it can be seen that current research on super-large-diameter tunnels primarily examines single-tunnel configurations, with limited studies on the dynamic response of twin tunnels.

In this paper, the factors affecting the static and dynamic response of the ultra-large-diameter twin tunnels (D = 15.2 m) are further investigated by DEM based on the previous research of our group [17]. Three parameters with different internal walls, different spacings, and different water pressures are set up, and the static and dynamic responses of sleepers, segments, and surroundings of super-large twin tunnels under train vibration are investigated. This research provides scientific guidance for the design, construction, and operation of super-large-diameter twin tunnel projects.

2. Modeling Procedure

2.1. Project Overview

This study is based on the Sanyang Road combined road-rail twin tunnels of Wuhan Metro Line 7, the cross section of this super-large-diameter (D = 15.2 m) twin tunnels as shown in Figure 1. The burial depth of twin tunnels is 0.5 D, and the water depth varies between 0.5 D and 1.5 D, with a minimum clear spacing of l = 0.25 D between the twin tunnels. The geometric dimensions of the tunnels and the physical–mechanical parameters of the surroundings (silty sand) are summarized in Tables 1 and 2. The Type A train, which operates in Wuhan Metro Line 7, and its corresponding train-induced vibration loads are illustrated in Figure 2. Detailed derivations of these loads can be found in the prior research [17].

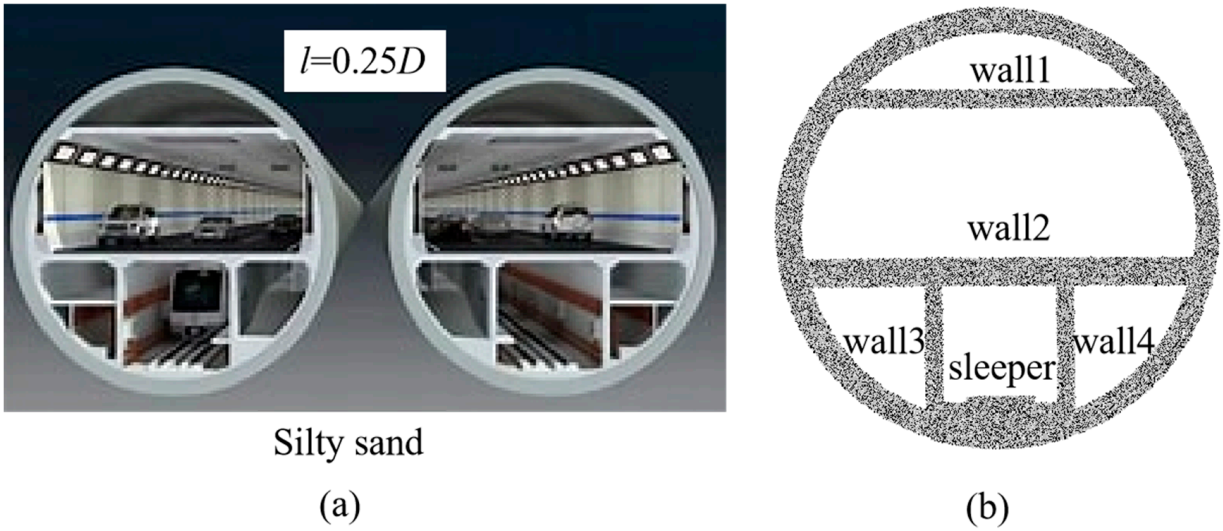


Figure 1. Cross section of super-large-diameter twin tunnels: (**a**) schematic diagram; (**b**) details of the cross-section of shield segments.

Table 1. Basic dimensions of twin tunnels model.

Model Parameter	Diameter	Thickness of Liner	Thickness of Wall1	Thickness of Wall2	Thickness of Wall3 and Wall4	Size of Sleeper (Length × Height)
Dimension (m)	15.2	0.65	0.65	1.0	0.65	1.2 × 0.2

Table 2. Physical–mechanical parameters of silty sand.

Silty Sand	w/%	E_s/MPa	c/kPa	φ/°	v	γ/kN/m^3
Physical and mechanical parameters	20.4	21.9	7.0	31.9	0.49	20

Note: w is the water content; Es is the compression modulus; c is the cohesion; φ is the friction; v is the Poisson's ratio; γ is the bulk density.

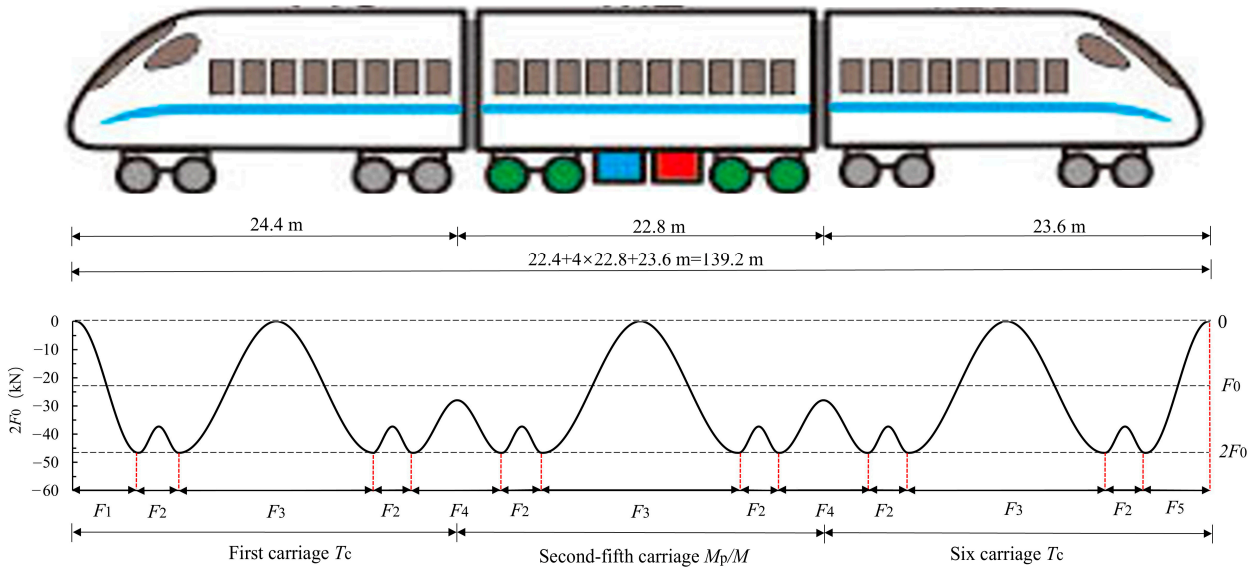


Figure 2. Type A metro train and its load time–history curve.

2.2. Basic Model Information

The discrete element method (DEM) establishes a physical and mechanical model of contact based on Newton's second law and the force-displacement equation to simulate discontinuous and discrete elements. This method has wide applicability and has been applied in fields such as mining [22,23], civil engineering, petroleum [24], chemical engineering [25,26], waste material isolation, agriculture [27,28], and materials science [29,30].

In this paper, the two-dimensional model recommended in the user manual is adopted for modeling. The modeling process is detailed in the literature [13]. The summary of mesoscopic parameters adopted for the surroundings and C60 segments is shown in Tables 3 and 4.

Table 3. Micro-parameters of silty sand in the DEM model.

Parameters	Radius of Particles (m)	Density (kg/m^3)	Normal Stiffness (N/m)	Tangential Stiffness (N/m)	Coefficient of Friction
Silty sand①	R_1 = 0.12–0.2	2000	2.05×10^7	2.05×10^7	0.62
Silty sand②	$R_2 = r_1$ = 0.06–0.1	2000	2.19×10^7	2.19×10^7	0.62
Silty sand③	r_2 = 0.03–0.05	2000	2.27×10^7	2.27×10^7	0.63

Table 4. Micro-parameters of C60 segments in the DEM model.

Parameters	C60①	C60②	Parameters	C60①	C60②
Radius of particles (m)	r_3 = 0.009–0.012	R_3 = 0.02–0.03	Normal strength of parallel bond (Pa)	7.1×10^9	6.9×10^9
Density (kg/m^3)	2500	2500	Tangential strength of parallel bond (Pa)	7.1×10^9	6.9×10^9
Normal stiffness (N/m)	9×10^8	9×10^8	Normal stiffness of parallel bonding (N/m)	9×10^8	8.6×10^8
Tangential stiffness (N/m)	9×10^8	9×10^8	Parallel bonding tangential stiffness (N/m)	9×10^8	8.6×10^8
Coefficient of friction	1.98	1.98	Parallel bonding radius	1.0	1.0

Note: C60① for small-diameter twin tunnels and C60② for large-diameter twin tunnels.

Three sets of numerical models were established to investigate the influencing factors of the dynamic response of super-large-diameter twin tunnels under train-induced vibrations. These models analyze the static and dynamic characteristics of adjacent tunnel liners and surroundings under different conditions, including internal wall configurations, absolute and relative spacings between tunnels, and varying water pressures. The model details are summarized in Table 5.

Table 5. Summary of model information.

No.	Objective	Condition	Explanation
1	Comparison of inner wall effects	A_1 (T2) A_2 (W234) A_3 (W12) A_4 (W2) A_5 (NW)	Super-large-diameter twin tunnels Super-large twin tunnels with wall2, wall3, and wall4 Super-large twin tunnels with wall1 and wall2 Super-large twin tunnels with wall2 Super-large twin tunnels with no internal walls
2	Comparison of absolute and relative spacing	B_1 B_2 B_3	Small-diameter twin tunnels with 0.25 *d* spacing Super-large twin tunnels with 0.25 *d* spacing Super-large twin tunnels with 0.25 *D* spacing
3	Comparison of water pressure	C_1 C_2 C_3	0.5 *D* water pressure 1.0 *D* water pressure 1.5 *D* water pressure

The first set comprises five models (T2, W234, W12, W2, and NW), and the cross-section of T2 is illustrated in Figure 3. The analysis primarily addresses the displacement and velocity of adjacent tunnel sleepers, liners, and surroundings under train loads.

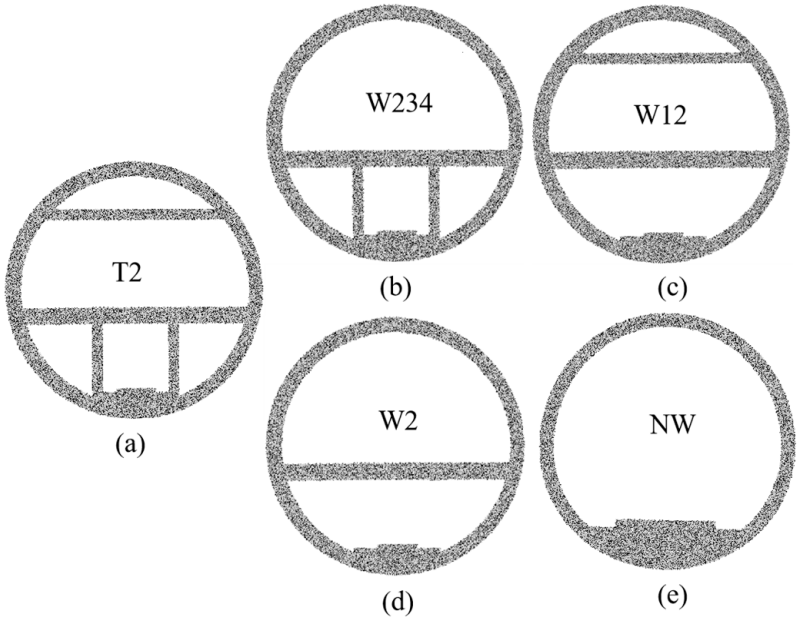


Figure 3. Five conditions of the first set of models: (**a**) A1; (**b**) A2; (**c**) A3; (**d**) A4; (**e**) A5.

The second set of models, comprising three conditions (B_1, B_2, and B_3), aiming to compare the absolute and relative spacing, are illustrated in Figure 4. The absolute spacing is defined as maintaining identical distances between the small and super-large twin tunnels, while relative spacing refers to controlling the ratio of the tunnel spacing to their respective diameters to be consistent.

The comparison between B_1 and B_2 aims to evaluate the influence of train-induced vibrations on adjacent tunnels under identical absolute spacing (0.25 d), whereas the comparison between B_1 and B_3 focuses on the effects under identical relative spacing. The spacing of the twin tunnel in B1-B3 conditions is calculated by Equations (1) and (2).

$$l_1 = l_2 = 0.25\,d = 0.25 \times 6.2\ \text{m} = 1.55\ \text{m} \quad (1)$$

$$l_3 = 0.25\,D = 0.25 \times 15.2\ \text{m} = 3.8\ \text{m} \quad (2)$$

where d is the diameter of small twin tunnels, and D is the diameter of super-large twin tunnels.

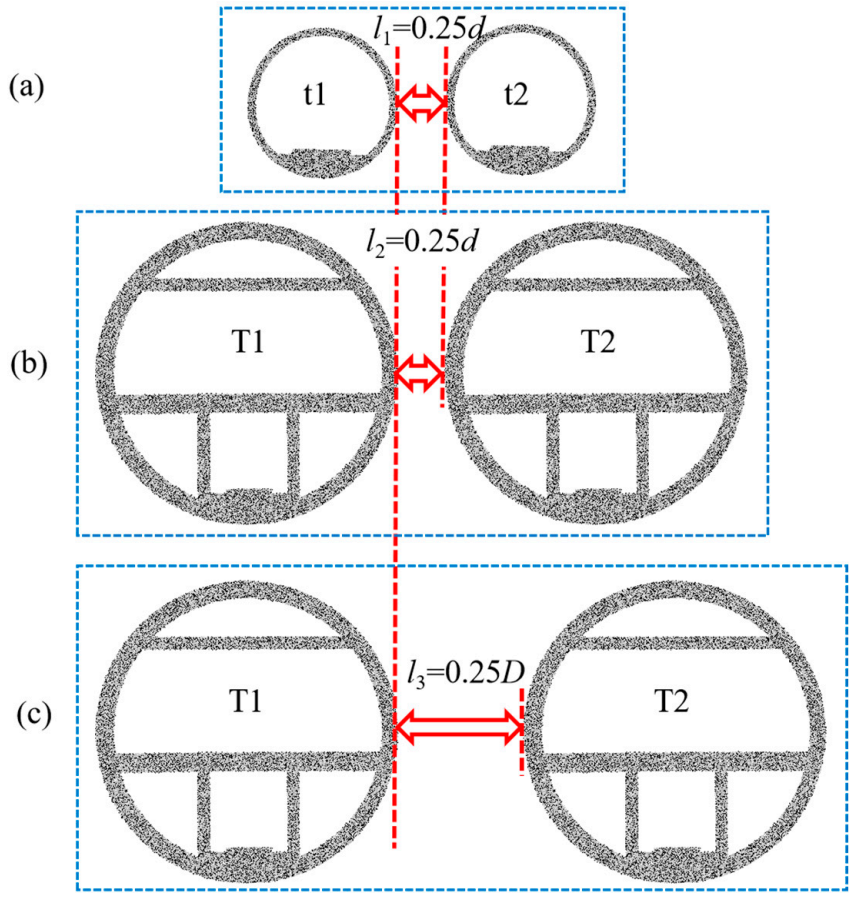


Figure 4. Three conditions of the second set of models: (**a**) B_1; (**b**) B_2; (**c**) B_3.

The third set of models includes three conditions, comparing the static and dynamic responses of the adjacent tunnel of super-large-diameter twin tunnels under train-induced vibrations at different water pressures. The water pressures on the top surface of the model for conditions C_1, C_2, and C_3 are 0.5 D, 1.0 D, and 1.5 D, respectively, and they are calculated by the following Equations (3)–(5):

$$C_1\text{: } P_1 = \rho g h_1 = 1 \times 10^3 \times 9.81 \times 0.5 \times 15.2 = 74.6 \text{ kPa} \quad (3)$$

$$C_2\text{: } P_2 = \rho g h_2 = 1 \times 10^3 \times 9.81 \times 1.0 \times 15.2 = 149 \text{ kPa} \quad (4)$$

$$C_3\text{: } P_3 = \rho g h_3 = 1 \times 10^3 \times 9.81 \times 1.5 \times 15.2 = 223 \text{ kPa} \quad (5)$$

where ρ is the density of water, 1 g/cm^3; g is gravitational acceleration, 9.81 m/s^2; and h_i (i = 1,2,3) is the depth of groundwater from the top surface of the model.

Taking the C_2 condition as an example, a schematic diagram of water pressure calculation for the C_2 condition in the third set of models can be seen in Figure 5. The length and height of the model are 64.6 and 38.0 m. The lateral pressure coefficient is specified as 0.4 [17]. The water pressures on all sides of the model are calculated as follows: Equations (6)–(8):

$$P_{w1} = \rho g h_2 = 149 \text{ kPa} \quad (6)$$

$$P_{w2} = P_{w1} + \rho g H = 149 + 1 \times 9.81 \times 38.0 = 522 \text{ kPa} \quad (7)$$

$$P_{w3} = P_{w4} = (P_{w1} + P_{w2}) \times 0.5 \times 0.4 = 134 \text{ kPa} \quad (8)$$

where P_{w1} is the water pressure on the top surface of the model; P_{w2} is the water pressure on the bottom surface of the model; and P_{w3} and P_{w4} are the water pressures on the left and right sides of the model.

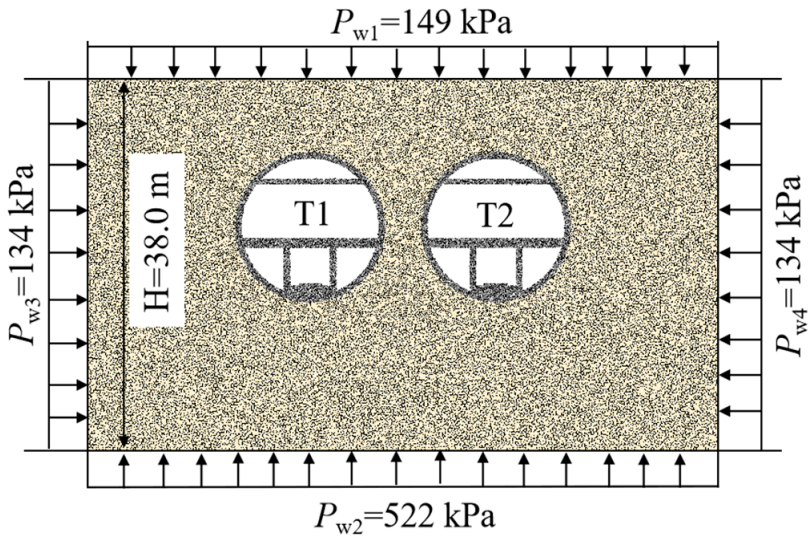


Figure 5. Schematic diagram of water pressure calculation for C_2 condition in the third set of models.

3. Results and Discussion

This chapter is divided into three subsections. Firstly, the vibration characteristics of adjacent super-large-diameter tunnels under train-induced vibrations under A_1–A_5 conditions (Figure 3), focusing on the analysis of displacement and velocity in tunnel sleepers, liners, and surroundings. Secondly, we compare the responses of liners and surroundings in adjacent tunnels under train-induced vibrations when the absolute and relative spacings between super-large and small twin tunnels are identical (Figure 4). Finally, we compare the maximum displacement and velocity of adjacent tunnel liners and surroundings under varying water pressure conditions (74.6 kPa, 149 kPa, 223 kPa) on the top face of super-large twin-tunnel models during train-induced vibrations.

3.1. Inner Walls

Super-large-diameter tunnels contain various inner walls: wall1 denotes the smoke exhaust board, wall2 represents the vehicular lane board, while wall3 and wall4 correspond to the left and right partition walls, respectively. This section focuses on investigating the static–dynamic response levels of these walls on adjacent tunnel sleepers, liners, and surroundings.

3.1.1. Sleeper

The horizontal displacement and velocity patterns of adjacent tunnel structures and surroundings are similar to their vertical counterparts, though the vertical displacement and vertical velocity (D_V and V_V) values consistently exceed horizontal measurements based on previous comparative studies [17]. Therefore, this study emphasizes the vertical responses of Tunnel 2 structures and surroundings.

Figure 6 illustrates the time–history curves of vertical displacement (D_V) and velocity (V_V) at the mid-point S_3 of Tunnel 2 sleepers under conditions A_1–A_5. S_1 and S_5 are the left and right endpoints, and S_2 and S_4 are the points of application of the train load. As train-induced vibrations propagate, the D_V and V_V values at S_3 exhibit oscillatory behavior under A_1–A_5 conditions, with the NW condition demonstrating significantly greater D_V and V_V compared to other conditions.

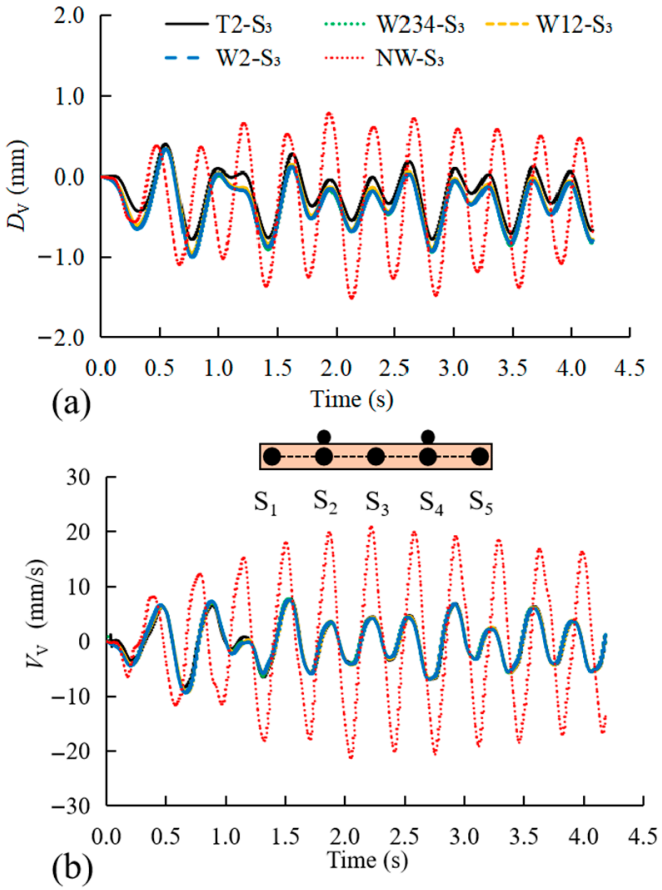


Figure 6. Time–history curves of D_V and V_V at point S_3 of T2 sleeper under A_1–A_5 conditions: (**a**) D_V; (**b**) V_V.

The D_V of point S_3 in T2 sleepers is shown in Figure 6a. The minimum and maximum values were −1.52 mm and 0.79 mm, respectively. The absolute values of negative D_V for S_3 were significantly larger than the positive values, indicating that the sleepers in adjacent tunnels primarily experience downward pressure under train loads.

The differences between maximum and minimum D_V values under the five conditions were 1.19 mm (T2), 1.31 mm (W234), 1.3 mm (W12), 1.34 mm (W2), and 2.31 mm (NW). The NW condition exhibited the largest amplitude, with a 94.12% increase compared to T2. At 2.13 s, the D_V reached −1.52 mm, showing distinct behavior from other conditions.

The D_V trends for W234, W12, W2, and T2 were similar, with nearly overlapping curves. Compared to T2, the amplitude increases for these conditions were 10.08%, 9.24%, and 12.61%, respectively. The absence of wall2 in NW led to its significantly higher D_V, confirming that wall2 plays a critical role in mitigating train-induced vibrations and maintaining tunnel stability.

The V_V of point S_3 in T2 sleepers is shown in Figure 6b. Under T2, W234, W12, and W2, the V_V curves overlapped, with maximum positive and negative peaks at 7.78 mm/s and −9.39 mm/s, respectively. In contrast, the NW condition showed an outstanding V_V trend, peaking at −21.35 mm/s (t = 2.05 s) and 20.87 mm/s (t = 2.22 s), followed by gradual stabilization.

The differences between maximum and minimum V_V values at A_1–A_5 conditions are 16.17 mm/s (T2), 16.99 mm/s (W234), 16.81 mm/s (W12), 16.95 mm/s (W2), and 42.35 mm/s (NW). Compared to T2, the increases were 5.07%, 3.96%, 4.82%, and 161.90%, respectively. This indicates that the internal walls of super-large tunnels significantly reduce

the V_V of adjacent tunnel sleepers, with wall2 playing a decisive role in mitigating the dynamic response of Tunnel 2 sleepers.

As shown in Figure 6a,b, the V_V curves largely overlap under A_1–A_4 conditions, while D_V exhibits some differences. This indicates that inner walls exert a greater influence on D_V than on V_V. Adjacent tunnel sleepers oscillate vertically under these vibrations because metro train-induced vibrations induce pronounced dynamic disturbances in closely spaced tunnels. Internal walls in super-large-diameter tunnels markedly reduce the static–dynamic responses of sleepers, with wall2 playing a decisive role. Notably, the NW condition exhibits the most severe sleeper disturbances, significantly exceeding other conditions.

To further investigate the displacement patterns of Tunnel 2 sleepers, Figure 7 compares the D_V and V_V variations in A_1–A_5 conditions. The calculation formulas are provided in Equations (9) and (10).

$$D_V = D_{Vmax} - D_{Vmin} \tag{9}$$

$$V_V = V_{Vmax} - V_{Vmax} \tag{10}$$

where D_{Vmax} is the maximum value of vertical displacement; D_{Vmin} is the minimum value of vertical displacement; V_{Vmax} is the maximum value of vertical velocity; and V_{Vmin} is the minimum value of vertical velocity.

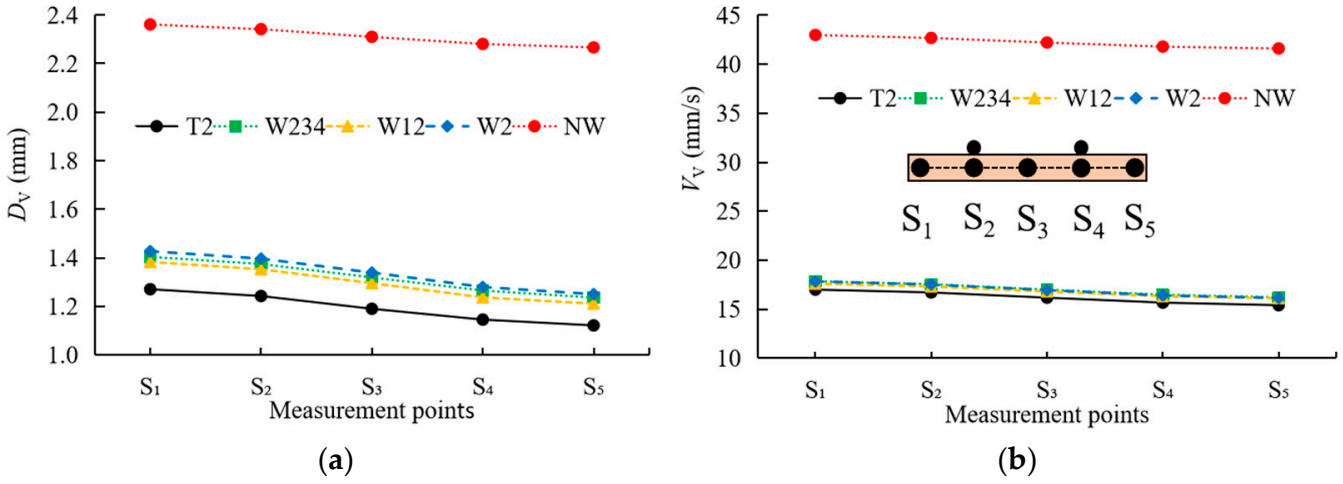


Figure 7. Comparison of D_V and V_V at S_1–S_5 points of Tunnel 2 sleepers: (**a**) D_V; (**b**) V_V.

The D_V variations at monitoring points of Tunnel 2 sleepers are shown in Figure 7a. The maximum and minimum D_V variations are 2.36 mm and 1.12 mm, respectively. Under the NW condition, D_V variations (2.27–2.36 mm) significantly exceed those of the other four conditions (1.12–1.43 mm), further confirming the decisive role of wall2 in reducing D_V. Comparing W12 and W234, the differences between S_1-S_5 monitoring points are 0.02, 0.02, 0.02, 0.03, and 0.03 mm, respectively. The slightly higher D_V variations in W234 indicate that horizontal wall1 contributes more to D_V reduction than vertical wall3 and wall4.

The V_V variations at monitoring points are shown in Figure 7b. The V_V curves nearly overlap (15.40–17.85 mm/s) under A_1–A_4 conditions, while NW exhibits significantly higher values (41.61–42.99 mm/s). Compared to T2, NW shows V_V variation increases of 152.97% (S_1), 155.48% (S_2), 161.10% (S_3), 166.75% (S_4), and 170.13% (S_5). This underscores wall2's dominant role in suppressing V_V, while wall1, wall3, and wall4 have negligible effects.

Compared to Figure 7a,b, point S_1 exhibits the largest D_V and V_V values, while point S_5 shows the smallest under A_1–A_5 conditions. This indicates that sleeper regions closer to T1 experience greater vertical vibration impacts. The effectiveness of internal walls in reducing D_V and V_V for Tunnel 2 sleepers is ranked as wall2 > wall1 > wall3 = wall4, with wall2 playing a decisive role.

As shown in Figures 6 and 7, adjacent tunnel sleepers oscillate vertically with train loads under metro train-induced vibrations. The D_V and V_V of Tunnel 2 sleepers under NW condition are significantly higher than other conditions, confirming that internal walls markedly reduce both static and dynamic responses. The stabilizing effect of Tunnel 2 internal walls follows the hierarchy: wall2 > wall1 > wall3 + wall4. Wall2 is critical for suppressing the static–dynamic characteristics of Tunnel 2 sleepers.

3.1.2. Liner

As shown in Figure 8, the maximum resultant displacements (D_R) and velocities (V_R) values at four monitoring points (0°, 90°, 180°, and 270°) of the Tunnel 2 liner vary significantly across the A_1–A_5 conditions. D_R and V_R are calculated by Equations (11) and (12).

$$D_R = \sqrt{D_h^2 + D_v^2} \tag{11}$$

$$V_R = \sqrt{V_h^2 + V_v^2} \tag{12}$$

where D_H is the maximum horizontal displacement; D_V is the maximum vertical displacement; V_H is the maximum horizontal velocity; and V_V is the maximum vertical velocity.

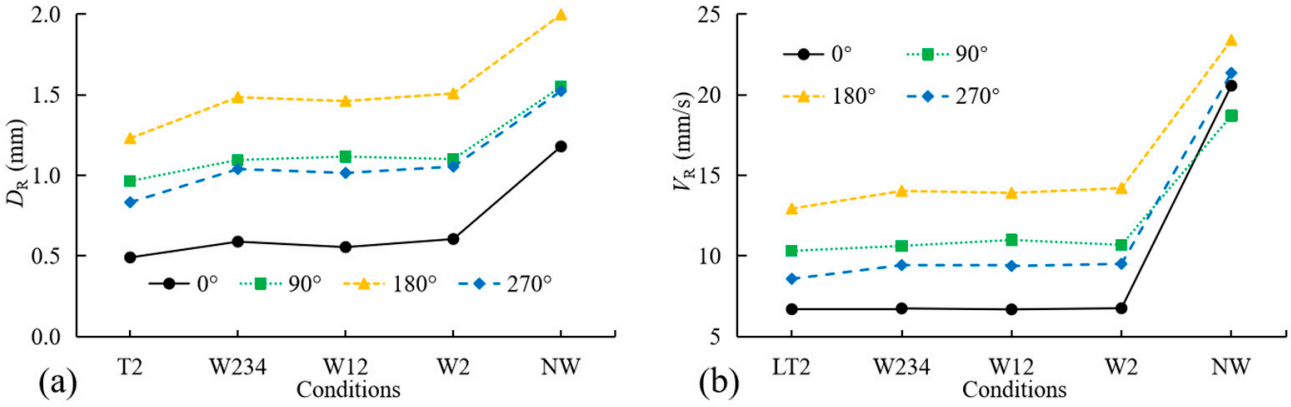


Figure 8. Comparison of maximum D_R and V_R at four monitoring points of Tunnel 2 liners under A_1–A_5 conditions: (**a**) D_R; (**b**) V_R.

As shown in Figure 8a, the maximum D_R values at the 0°, 90°, 180°, and 270° monitoring points of the Tunnel 2 liner vary significantly under A_1–A_5 conditions. D_R magnitudes follow the order 180° > 90° > 270° > 0° across all conditions, reflecting distinct vibration impacts at each angle. The largest D_R consistently occurs at 180° (closest to T1), while the smallest D_R is observed at 0° (farthest from T1). D_R attenuates progressively from the vibration source (180°) toward the opposite side (0°), demonstrating a clear distance-dependent decay pattern. Notably, D_R at 270° is slightly smaller than at 90°, indicating that deeper burial depth enhances structural restraint from the surroundings, thereby improving the liner's resistance to disturbances and reducing displacements. This highlights two key factors influencing D_R: (1) proximity to the vibration source and (2) burial depth, with deeper sections benefiting from stronger soil support to mitigate displacement.

The maximum V_R values of the Tunnel 2 liner are shown in Figure 8b. Under conditions with internal walls, the V_R trends align with the D_R patterns in Figure 8a, following the order 180° > 90° > 270° > 0°, further confirming that V_R increases with proximity to the vibration source (T1). However, under the NW condition, the V_R ranking shifts to 180° > 270° > 0° > 90°. This anomaly likely stems from the reduced structural stability of the liner without internal walls, making it more susceptible to vibrations from T1 and resulting in markedly different velocity patterns compared to wall-equipped conditions.

Under train-induced vibrations, both D_R and V_R at the four monitoring points of Tunnel 2 liner correlate strongly with distance from the vibration source and burial depth. The NW condition exhibits distinct D_R and V_R patterns (e.g., reversed ranking at 270° and 0°) and significantly higher magnitudes compared to other conditions, emphasizing the critical role of internal walls in stabilizing dynamic responses.

3.1.3. Surroundings

The surroundings play a critical role in supporting tunnel structures to maintain stability under dynamic loads. Analyzing the dynamic characteristics of the surroundings provides essential insights to complement the dynamic behavior of Tunnel 2 liners.

Figure 9 shows the D_R and V_R of Tunnel 2 surroundings under A_1–A_5 conditions. Figure 9a compares the maximum D_R values of the T2 surroundings. The D_R magnitudes at four monitoring points follow the order 180° > 90° > 270° > 0°, consistent with the trends observed in Figure 8a. This confirms that the D_R of surroundings is similarly influenced by propagation distance from the vibration source and burial depth.

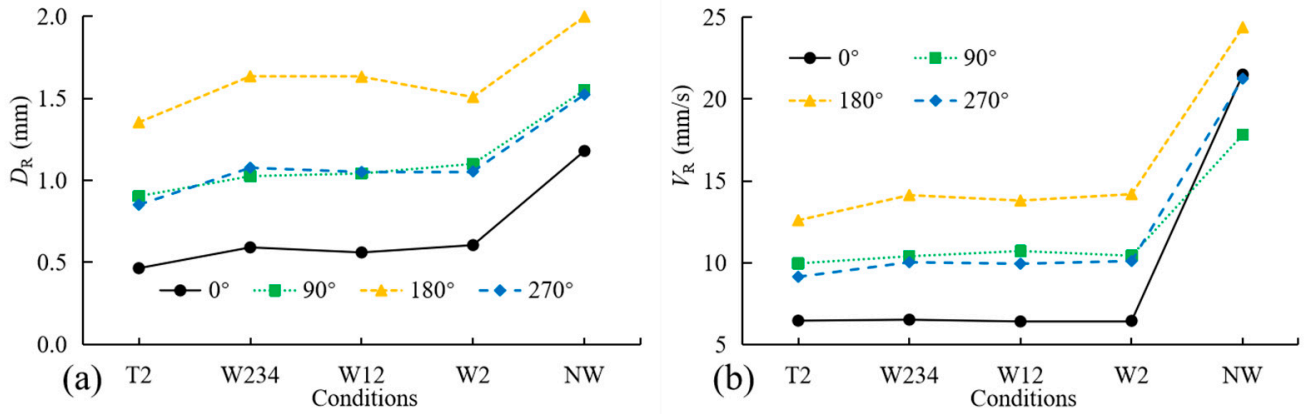


Figure 9. Comparison of maximum D_R and V_R in surroundings under A_1–A_5 conditions: (**a**) D_R; (**b**) V_R.

Figures 8a and 9a reveal minimal differences in D_R between Tunnel 2 liners and surroundings across A_1–A_5 conditions. Notably, the D_R values at four angles (0°, 90°, 180°, 270°) are identical for both liners and surroundings under W2 and NW conditions, indicating that the displacement patterns of tunnel structures and surroundings are closely aligned under metro train-induced vibrations, signifying a structurally safe state.

Comparing T2 and NW conditions, the differences of D_R in surroundings at 180° and 0° are 0.65 mm and 0.71 mm under the T2 condition are increased by 48.15% and 151.06% when compared to the NW condition. These results demonstrate that internal walls significantly reduce D_R in surroundings, with effectiveness varying by proximity to the vibration source.

Figure 9b compares the maximum V_R values of the Tunnel 2 surroundings under A_1–A_5 conditions. Similar to the D_R trends in Figure 9a and the liner V_R patterns in Figure 8b, the V_R magnitudes under A_1–A_5 conditions follow 180° > 90° > 270° > 0° which is consistence with the D_R trends in Figure 9a and the liner V_R patterns in Figure 8b, confirming that V_R increases with proximity to the vibration source, consistent with findings from liner analysis.

Under the NW condition, the V_R ranking shifts to 180° > 0° > 270° > 90°, deviating from the established patterns observed in wall-equipped conditions. This indicates that the vibration transmission law identified in Figure 8b does not apply to NW condition.

Compared to the most stable condition T2, the V_R differences in surroundings at 180° and 0° under NW condition are 11.79 mm/s and 15.03 mm/s, increased by 93.57% and 230.30% when compared to the value in the most stable condition T2. This indicates that the absence of internal walls (NW) leads to significantly amplified and complex dynamic responses in both liners and surroundings under dynamic loads, further proving the critical role of internal walls in stabilizing the surroundings.

As shown in Figure 9a, b, the D_R and V_R patterns in the surroundings at four monitoring points align closely with those of the liners, governed by their position, proximity to the vibration source, and burial depth. Additionally, the T2 condition exhibits the highest stability, and the internal walls significantly reduce the D_R and V_R of the surroundings when comparing T2 and NW conditions. Notably, wall2 contributes most prominently to maintaining the stability of the surroundings.

Figure 10 shows the coordination of the surroundings at various angles of Tunnel 2 under T2 and NW conditions. Coordination is defined as the average number of particles in contact with a central particle within a measurement circle, which can reflect structural stability. A higher coordination means greater stability. Each tunnel is monitored via eight measurement circles (0°, 45°, 90°, 135°, 180°, 215°, 270°, and 315°) to assess coordination at different angles. Changes in the coordination of Tunnel 2 surroundings indicate the disturbance level induced by train-induced vibrations from the adjacent tunnel.

Under the NW condition, coordination variations at all monitoring points are greater than those under T2. The most significant coordination changes occur at the vault (90°), followed by 180°, indicating that coordination changes in the Tunnel 2 surroundings correlate with monitoring distance and position. At the vault, train-induced vibrations cause particles to slide downward along the liners, leading to a decrease in coordination and stability, which also shows that the vault is the focus of dynamic characteristics.

Overall, the Tunnel 2 surroundings exhibit greater fluctuations in coordination under NW condition due to the absence of internal walls when compared to the T2 condition. Under T2 condition, the surroundings with greater burial depth demonstrate higher coordination, which remains nearly constant throughout the testing period. This indicates that the lower-right region of the Tunnel 2 surroundings is less affected by vibrations and maintains greater stability.

Combined with Figures 9 and 10, the static–dynamic responses of Tunnel 2 surroundings are influenced by the position of liners and surroundings, proximity to the vibration source, and burial depth. Internal walls enhance surroundings stability, while coordination is governed by distance from the vibration source and burial depth. The T2 condition demonstrates higher and more stable coordination, highlighting the structural benefits of internal walls.

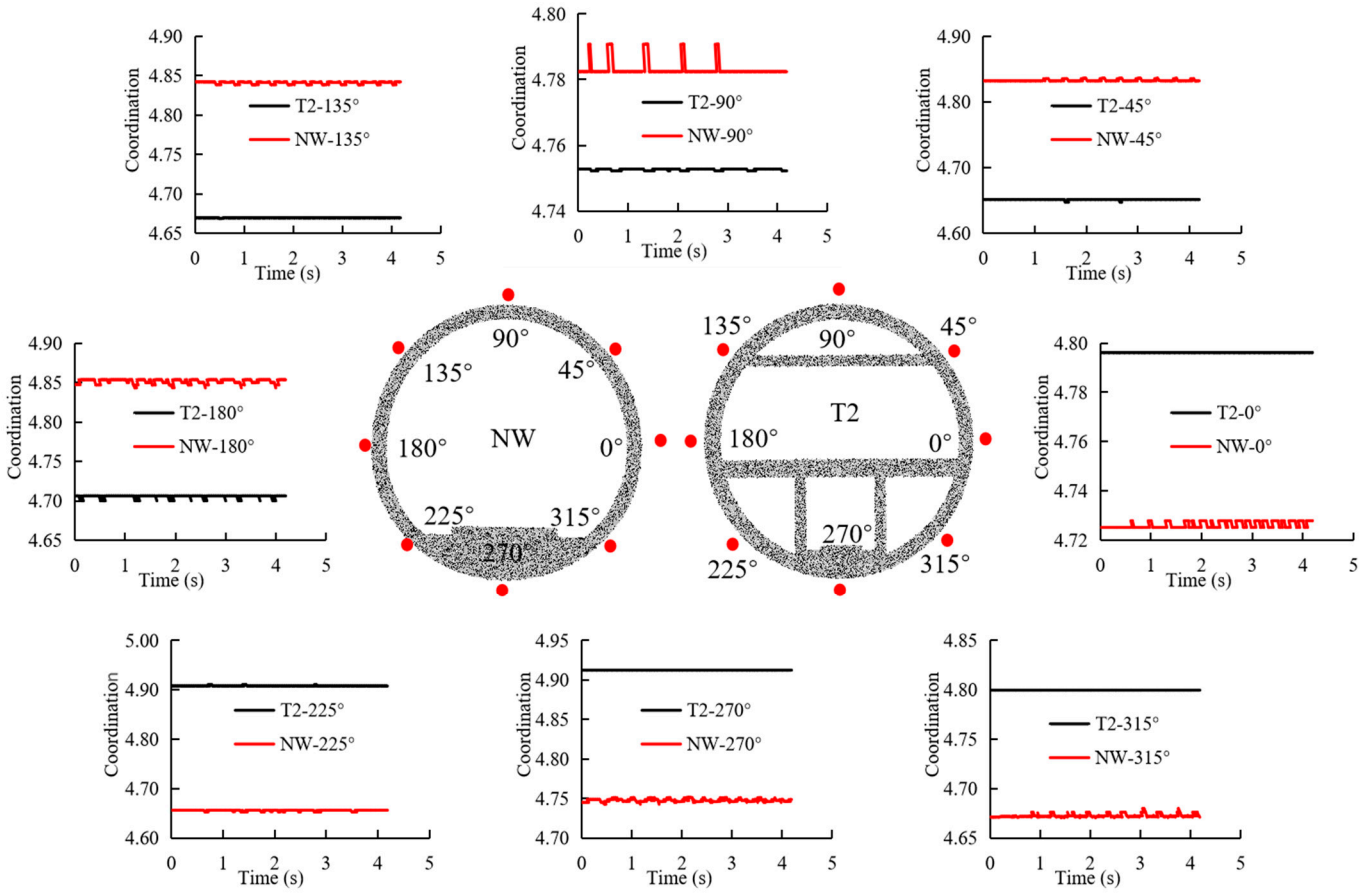


Figure 10. Comparison of coordination in Tunnel 2 surroundings at various angles under A_1–A_5 conditions.

3.2. Absolute and Relative Spacing

It is well-known that the spacing between parallel twin tunnels significantly influences the dynamic characteristics of the adjacent tunnel [31–33]. Figure 11 compares the D_R and V_R of adjacent tunnel liners and surroundings under varying spacing conditions to investigate the effects of absolute and relative spacing.

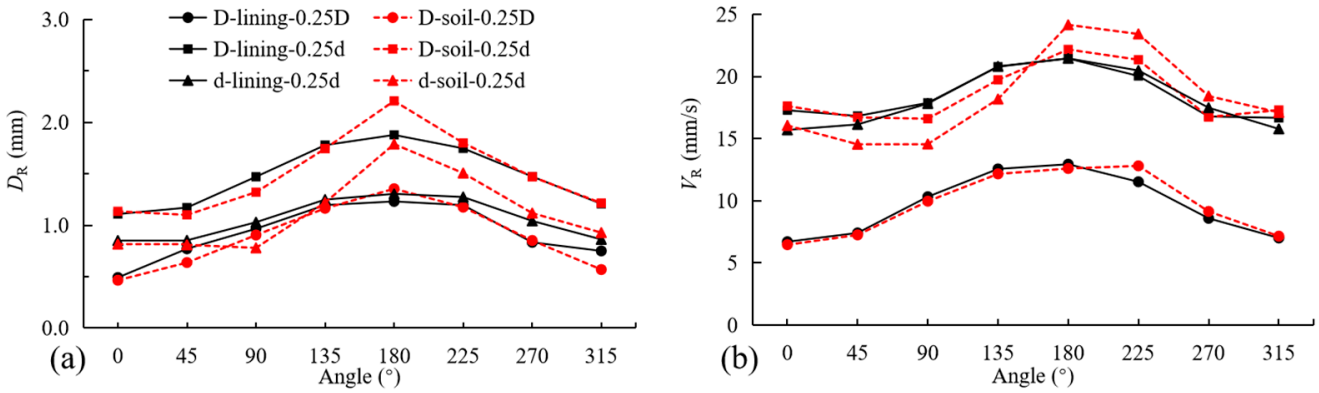


Figure 11. Comparison of D_R and V_R in adjacent tunnel liners and surroundings under B_1–B_3 conditions: (**a**) D_R; (**b**) V_R.

As shown in Figure 11a, the maximum and minimum differences of D_R of liners and surroundings under B_1–B_3 conditions occur at 180° (closest to T1), confirming that proximity to the vibration source dominates displacement patterns. The maximum liner-surroundings D_R differences for B_1, B_2, and B_3 are 0.49 mm, 0.33 mm, and 0.12 mm. Such discrepancies possibly destabilize the surroundings due to insufficient structural support.

The liners D_R ranking is as follows: $B_2 > B_1 > B_3$. For the surroundings, all other monitoring points align with the same ranking of the liners except at the vault (90°), where the D_R of the small-diameter tunnels is slightly lower than that of the 0.25 D super-large-diameter tunnels. This indicates that super-large-diameter tunnels exhibit greater static–dynamic responses under the same absolute spacing while showing slightly lower responses under relative spacing equivalence. Additionally, the granular nature of the surroundings leads to distinct displacement patterns at the vault compared to other monitoring points, necessitating focused stability assessments in this region.

As shown in Figure 11b, the V_R of liners and surroundings for the 0.25 D super-large-diameter twin tunnels (B_3) is significantly smaller than those under B_1 and B_2 conditions. This indicates that the dynamic characteristics of super-large-diameter tunnels with equivalent relative spacing (B_3) are markedly lower compared to small-diameter tunnels (B_1) and super-large-diameter tunnels with 0.25 d (B_2). Additionally, the V_R of surroundings and liners align closely across all monitoring points, suggesting that the surroundings effectively support the tunnel structure, placing the super-large-diameter tunnel in a safer state.

Comparing B_1 and B_2 conditions, significant V_R differences exist between surroundings and liners. In the 45–135°, the V_R in surroundings is smaller than the value in liners, while in the 180–270°, the V_R in surroundings exceeds the value in liners. This opposing dynamic behavior in the upper-right and lower-left regions of Tunnel 2 disrupts the support mechanism between surroundings and liners, potentially leading to liner cracking, leakage, or instability.

The V_R in liners for super-large and small-diameter tunnels overlap at most monitoring points, with minor differences at 0°, 45°, and 315°. However, the V_R in surroundings exhibits substantial disparities. In the 0–135° interval (upper half), super-large-diameter tunnels (B_2) show higher V_R than small-diameter tunnels (B_1), while in the 180–270° interval (lower-left corner), small-diameter tunnels (B_1) exhibit higher V_R. This demonstrates that under equivalent absolute spacing, liner displacements are comparable between super-large and small-diameter tunnels, but the V_R differences in surroundings are pronounced, highlighting distinct dynamic behaviors in super-large-diameter tunnel surroundings that warrant further investigation.

As shown in Figure 11a,b, the D_R and V_R of liners and surroundings follow the order $B_2 > B_1 > B_3$. For twin tunnels with equivalent relative spacing, super-large-diameter tunnels exhibit smaller static–dynamic responses in both liners and surroundings compared to small-diameter tunnels, likely attributed to the vibration-damping effect of internal walls discussed in Section 3.1. In contrast, under equivalent absolute spacing, super-large-diameter tunnels demonstrate significantly enhanced dynamic responses, accompanied by increased discrepancies in displacements and velocities between liners and surroundings. Regardless of whether absolute or relative spacing is maintained, the static–dynamic characteristics of super-large-diameter tunnel liners and surroundings fundamentally differ from those of small-diameter tunnels. This highlights the complex interactions between structural and surroundings in super-large-diameter tunnels, necessitating further research to address their unique challenges in stability and dynamic performance.

3.3. Water Pressure

Under train-induced vibrations, the surrounding water pressure of super-large-diameter twin tunnels exerts varying influences on adjacent tunnel liners and surroundings. This section investigates the static–dynamic responses of liners and surroundings under different water pressures (P_1 = 74.6 kPa, P_2 = 149 kPa, P_3 = 223 kPa).

Figure 12a compares the maximum D_R values under different water pressures (C_1–C_3 conditions). The D_R of liners and surroundings at C_2 condition is slightly smaller than at C_1 condition, while D_R at C_3 condition exceeds that at C_2 condition. This suggests that moderate water pressure (P_2 = 149 kPa) can mitigate train-induced vibrations in adjacent tunnels, whereas excessive water pressure (P_3 = 223 kPa) possibly amplifies displacements.

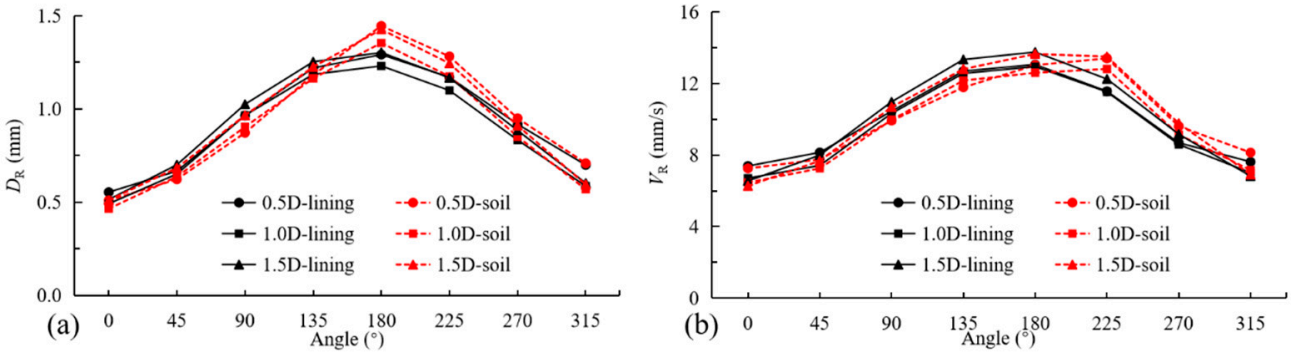


Figure 12. Comparison of maximum D_R and V_R at characteristic points of liners and surroundings under C_1–C_3 conditions: (**a**) D_R; (**b**) V_R.

Figure 12b compares the maximum V_R values. Across all monitoring points (0–315°), V_R initially increases and then decreases, peaking at 180° and 225°. The higher V_R in the central tunnel region (90–270°) correlates with proximity to the vibration source. From 0° to 180°, the liner V_R exceeds the surroundings V_R, while the reverse occurs from 180 to 315°, indicating that the distance to the vibration source significantly influences velocity distributions.

As shown in Figure 12a, b, the D_R and V_R of liners and surroundings remain similar for most monitoring points under C_1–C_3 conditions, with only minor variations observed at specific points such as 180° and 225°. The maximum displacement occurs at 180°, while peak velocity appears at 225°, indicating a spatial shift between the locations. Both displacement and velocity patterns are closely tied to proximity to the vibration source. Moderate water pressure (P_2 = 149 kPa) effectively reduces the static–dynamic responses of adjacent tunnel liners and surroundings under train-induced vibrations.

Figure 13a compares the average coordination of the surroundings. The results show significantly lower coordination under the C_1 condition compared to the C_2 and C_3 conditions. This demonstrates that increasing water pressure from 74.6 kPa to 149 kPa substantially enhances surroundings stability, particularly in the central tunnel region, where coordination at 180° increases by up to 9.81%. Under the C_3 condition, coordination improvements over the C_2 condition are marginal, indicating comparable stability levels between these two pressure conditions.

The coordination variation rate is defined as in Equation (13), and its change rate of the surroundings is shown in Figure 13b. Under the C_3 condition, the variation rate reaches its maximum at 180°, indicating significant instability in this region. The higher variation rate at the C_3 condition reflects reduced stability in the tunnel and surroundings

due to excessive water pressure, which increases stress in the twin tunnel structure and compromises stability.

$$A = \frac{M1 - M2}{M1} \times 100\% \quad (13)$$

where M_1 is the maximum coordination, and M_2 is the minimum coordination.

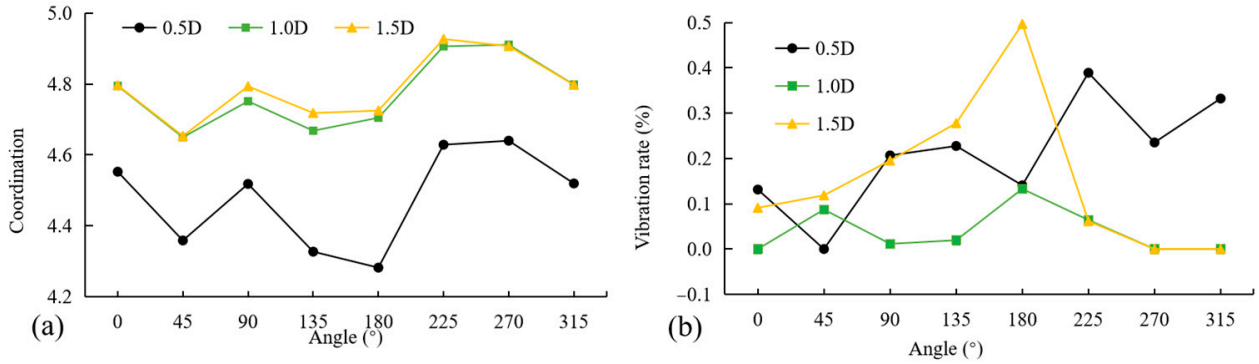


Figure 13. Comparison of coordination at characteristic points of surroundings under C_1–C_3 conditions: (**a**) average coordination; (**b**) coordination variation rates.

As shown in Figure 13a,b, the C_2 condition exhibits the highest stability among the three conditions. The central region of the twin tunnels (particularly at 180°) experiences the greatest impact. Optimal water pressure (P_2 = 149 kPa) effectively enhances the stability of super-large-diameter tunnels.

The displacements and velocities at the vault of super-large-diameter tunnels are significantly larger and exhibit distinct patterns compared to other monitoring points, necessitating focused investigation from Figures 11a and 12a. Figure 14a compares the vertical strain at the vault under different water pressures. The vertical strain curves oscillate with metro train-induced vibrations but remain positive, indicating vertical elongation of particles and soil loosening. This phenomenon arises because the surroundings at the vault tend to slide laterally due to the structural features of the liners under vibrations. Under C_2 and C_3 conditions, the vertical strains at the tunnel crown are similar and smaller than those at the C_1 condition, likely due to higher confining pressure in this region, which restricts particle movement and reduces strain.

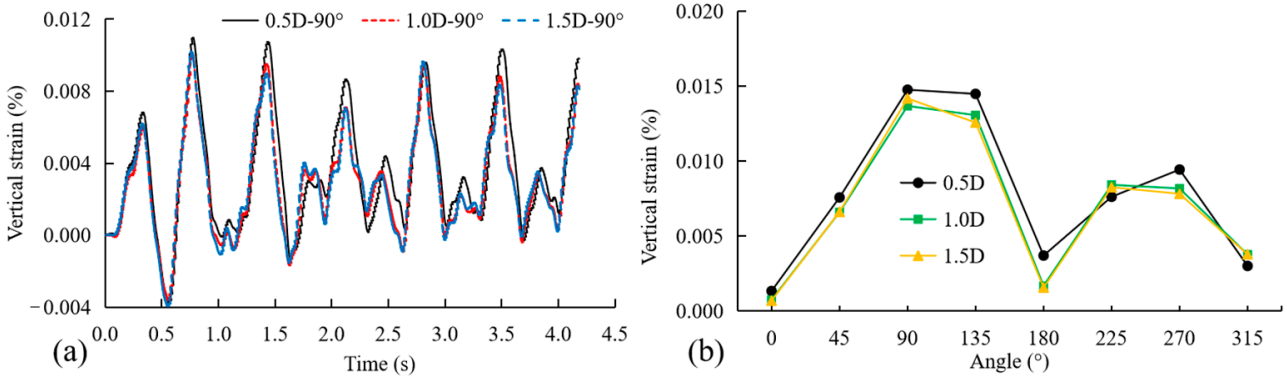


Figure 14. Comparison of vertical strain at characteristic points of surroundings: (**a**) vertical strain at 90°; (**b**) difference between maximum and minimum vertical strain.

Figure 14b compares the maximum and minimum values of vertical strain at the vault. Under C_1–C_3 conditions, the maximum vertical strain differences occur at 90° (0.015%, 0.014%, and 0.014%), while the minimum differences appear at 180° (0.004%, 0.002%, and 0.002%). This is likely due to the structural constraints of the twin tunnels at 180°,

which limit lateral particle movement, resulting in minimal vertical strain. At 135°, strain differences are slightly smaller than at 90°, possibly because this region is closer to both the vibration source (T1) and the vault. These points are experiencing stronger disturbances and weaker resistance to sliding, leading to higher vertical strain.

As shown in Figure 14a,b, the structural features of the vault liners cause significant positive vertical strain in the surroundings. Larger differences in maximum-minimum strains at 90° and 135° indicate lower stability in these regions.

As shown in Figures 12–14, increasing water pressure from C_1 to C_2 condition reduces the static–dynamic responses in super-large-diameter tunnels reduced when water pressure increase from C_1 to C_2 condition, while the static–dynamic responses increase when the water pressure further increases to C_3 condition. Optimal water pressure (P_2 = 149 kPa) is critical for maintaining stability. Displacement and velocity in the surroundings depend on proximity to the vibration source, with the central tunnel region (especially 180°) most affected. Vertical strain peaks at 90° and 135° require special attention due to their instability.

4. Conclusions

This study conducted a parametric analysis of the static–dynamic characteristics of adjacent tunnels for super-large-diameter twin tunnels under train-induced vibrations using the DEM. Three sets of models were developed to investigate the effects of internal walls, absolute and relative spacing, and water pressure on the static–dynamic responses of adjacent tunnel structures and surroundings. The main conclusions are as follows:

1. The NW condition (no internal walls) of T2 exhibits significantly greater static–dynamic responses in both liners and surroundings compared to other conditions. Internal walls in super-large tunnels markedly reduce these responses, with their stabilizing effectiveness ranked as wall2 > wall1 > wall3 = wall4. Wall2 plays a particularly decisive role. D_R and V_R in liners and surroundings correlate strongly with the burial depth and distance to the vibration source.
2. Under equivalent relative spacing, super-large twin tunnels show smaller static–dynamic responses in liners and surroundings than small twin tunnels. However, under equivalent absolute spacing, super-large twin tunnels exhibit significantly enhanced dynamic responses and larger discrepancies in liner and surroundings displacements and velocities. The static–dynamic characteristics of super-large twin tunnels fundamentally differ from those of small twin tunnels under any spacing.
3. Optimal water pressure (P_2 = 149 kPa) effectively suppresses displacements and velocities in liners and surroundings, while excessive pressure (P_3 = 223 kPa) amplifies static–dynamic responses. Critical monitoring points requiring attention include the central tunnel region (180°), vault (90°), and 135°, where responses are most pronounced due to proximity to the vibration source and the surroundings easily sliding.

The static–dynamic characteristics of super-large-diameter twin tunnel liners and surroundings differ fundamentally from those of small twin tunnels, highlighting the complex interactions between their liners and surroundings. Future research will employ the scale model to explore the dynamic behavior of super-large twin tunnels under train-induced vibrations.

Author Contributions: Conceptualization, L.W. and X.B.; methodology, L.W.; software, Z.C.; validation, L.W., X.B. and Z.C.; formal analysis, L.W.; investigation, X.B.; resources, H.G.; data curation, H.G.; writing—original draft preparation, Z.C.; writing—review and editing, L.W.; visualization, Z.C. and J.W.; supervision, H.G.; project administration, X.B.; funding acquisition, X.B. All authors have read and agreed to the published version of the manuscript.

Funding: National Natural Science Foundation of China (52208403, 52478359) and the Scientific Research Fund of Wuhan Institute of Technology (K202221).

Institutional Review Board Statement: Not applicable.

Informed Consent Statement: Not applicable.

Data Availability Statement: The original contributions presented in this study are included in the article. Further inquiries can be directed to the corresponding author.

Conflicts of Interest: The authors declare no conflicts of interest.

Nomenclature

D	Diameter of the large and super-large twin tunnels
d	Diameter of the small twin tunnels
t1	First small tunnel
t2	Second small tunnel
T1	First super-large-diameter tunnel
T2/Tunnel 2	Second super-large-diameter tunnel
D_V	Vertical displacement
D_R	Resultant displacement
V_V	Vertical velocity
V_R	Resultant velocity
wall1	Smoke exhaust board
wall2	Vehicular lane board
wall3	Left partition wall
wall4	Right partition wall
DEM	Discrete Element Method
l, l_1, l_2, l_3	Spacing between twin tunnels

References

1. Yang, W.; Yang, L.; Liang, Y.; Qian, Z.; Guo, W.; He, C.; Zhou, Y. Study on the Dynamic Response Characteristics of Road-metro Tunnels and Surrounding Soil under Train Vibration Loads. *Chin. J. Rock Mech. Eng.* **2022**, *41*, 1659–1670. [CrossRef]
2. Yu, T.; Ying, K.; Wang, J.; Yao, Z.; Fang, Y. Stability Evaluation of the Sequential Excavation Method of Large-Section Double-Arch Tunnel in Fly Ash Accumulation Stratum Through Physical Model. *Tunn. Undergr. Space Technol.* **2025**, *158*, 106391. [CrossRef]
3. Heidary, R.; Esmaeili, M.; Nik, M.G. Effects of Train Operational Parameters on Ground-Borne Vibrations Induced by Twin Metro Tunnels. *Int. J. Rail Transp.* **2020**, *9*, 144–156. [CrossRef]
4. Zhou, Y.; Yang, W.; Yao, C.; Xu, Z. Centrifuge Modelling of the Dynamic Response of Twin Tunnels Under Train-Induced Vibration Load. *Soil Dyn. Earthq. Eng.* **2024**, *185*, 108908. [CrossRef]
5. Li, L.; Yao, A. Investigation on Response of Site of Typical Soil–Rock Composite Strata in Changchun Induced by Shield Construction of Parallel Twin Tunnels. *Appl. Sci.* **2024**, *14*, 500. [CrossRef]
6. Pang, Y.; Lin, H.; Cao, P.; Meng, G. The Influence of Overlying High-Speed Rail Dynamic Loads on the Stability of Shield Tunnel Faces During Excavation. *Appl. Sci.* **2025**, *15*, 2567. [CrossRef]
7. Li, J.; Fang, X.; Yang, Y. Analysis of the Impact of the New Two-Lane Shield Tunnel Underpass on the Existing Tunnels. *Appl. Sci.* **2025**, *15*, 2642. [CrossRef]
8. Wang, Y.-c.; Guo, Y.; Qiu, Y.; Jiang, W.; Li, Y.-h.; Cheng, C. Dynamic Behavior of Fault Tunnel Lining Under Seismic Loading Conditions. *J. Cent. South Univ.* **2023**, *30*, 584–598. [CrossRef]
9. Liu, X.; Zhang, R.; Fang, Q.; Li, Q.-q.; Jiang, A.-n.; Li, K.-c. Subgrade Settlements of Existing Railway Lines and Operational Parameters of Shield Machine Induced by Twin Shield Tunnel Excavations: A Case Study. *J. Cent. South Univ.* **2024**, *31*, 272–287. [CrossRef]
10. Zhang, D.; Liu, Z.; Shen, G.; E, J. Measurement of Earth Pressure of Shallow Buried Tunnel with Super Large Diameter and Applicability Evaluation of Calculation Method. *Rock Soil Mech.* **2019**, *40*, 91–98. [CrossRef]
11. Amjadi, A.H.; Johari, A. Stochastic Nonlinear Ground Response Analysis Considering Existing Boreholes Locations by the Geostatistical Method. *Bull. Earthq. Eng.* **2022**, *20*, 2285–2327. [CrossRef]

12. Johari, A.; Amjadi, A.H.; Heidari, A. Stochastic Nonlinear Ground Response Analysis via a Case Study Site in Shiraz City. *Sci. Iran.* **2021**, *28*, 2070–2086. [CrossRef]
13. Li, C.; Zhang, W.; Wang, X.; Pan, B.; Zhu, H.-H.; Spencer, B.F. Modeling Dynamic Responses of a Cross-River Road Shield Tunnel Under Stochastic Vehicle Loads. *Tunn. Undergr. Space Technol.* **2020**, *102*, 103432. [CrossRef]
14. Zhang, S.; Yuan, Y.; Li, C.; Yang, Y.; Yu, H.; Mang, H.A. Effects of Interior Structure as Double Deck Lanes on Seismic Performance of Segmental Linings. *Tunn. Undergr. Space Technol.* **2020**, *103*, 103441. [CrossRef]
15. Shi, J.-K.; Zhang, J.-Z.; Zhao, S.; Guan, Z.-C.; Huang, H.-W. Probabilistic Analysis of Ground Surface Settlement Induced by Super Large Diameter Shield Tunneling Based on 3D Random Finite Element Method. *Comput. Geotech.* **2025**, *181*, 107111. [CrossRef]
16. Kou, L.; Xiong, Z.; Cui, H.; Zhao, J. Study on Mechanical Characteristics of Segmental Joints of a Large-Diameter Shield Tunnel under Ultrahigh Water Pressure. *Sensors* **2021**, *21*, 8392. [CrossRef] [PubMed]
17. Wu, L.; Zhang, X.; Wang, W.; Meng, X.; Guo, H. Comparison of Dynamic Characteristics between Small and Super-Large Diameter Cross-River Twin Tunnels under Train Vibration. *Appl. Sci.* **2021**, *11*, 7577. [CrossRef]
18. Wang, S.; He, X.; Peng, X.; Wang, Y.; Li, Z.; Song, Z. Influence of Secondary Lining Thickness on Mechanical Behaviours of Double-Layer Lining in Large-Diameter Shield Tunnels. *Undergr. Space* **2024**, *18*, 130–150. [CrossRef]
19. Guo, W.; Yang, W.; Qian, Z.; Yang, L.; He, C.; Qu, S. The Effect of Internal Structure on Dynamic Response of Road-Metro Tunnels Under Train Vibration Loads: An Experimental Study. *Tunn. Undergr. Space Technol.* **2023**, *138*, 105182. [CrossRef]
20. Li, Y.; Zou, Z. Numerical Investigation on the Influence of Super-Large-Diameter Shield Tunneling on Nearby Existing Metro Tunnels and the Protection Scheme. *Appl. Sci.* **2023**, *13*, 3179. [CrossRef]
21. Zhang, X.; Zhang, M.; Javadi, A.A. Influence of a Super-Large Diameter Shield Tunnel Excavation on the Lining Structure of the Metro Lines in Operation. *Iran. J. Sci. Technol. Trans. Civ. Eng.* **2023**, *47*, 3851–3866. [CrossRef]
22. Deng, L.; Lu, H.; Liu, S.; Hu, Q.; Yang, J.; Kang, Y.; Sun, P. Particle Anti-Accumulation Design at Impeller Suction of Deep-Sea Mining Pump and Evaluation by CFD-DEM Simulation. *Ocean Eng.* **2023**, *279*, 114598. [CrossRef]
23. Yang, W.; Ge, F.; Chen, X.; Wang, L.; Ma, P.; Xu, Z. Optimization of Collection Efficiency for a Dual-Row Jet Mining Machine Based on CFD-DEM Coupling. *Ocean Eng.* **2024**, *313*, 119633. [CrossRef]
24. Wang, X.; Gong, L.; Li, Y.; Yao, J. Developments and Applications of the CFD-DEM Method in Particle–Fluid Numerical Simulation in Petroleum Engineering: A Review. *Appl. Therm. Eng.* **2023**, *222*, 119865. [CrossRef]
25. Lapshin, O.V.; Polyakov, I.S.; Boyangin, E.N. Macrokinetics of Mixing Binary Powder Compositions, Augmented by the DEM Method and Experimental Studies on the Chemically Reactive System 3Ni–Al. *Powder Technol.* **2025**, *460*, 121074. [CrossRef]
26. Nadda, M.; Banaeizadeh, A.; Avilala, P.; Roy, S.; Yadav, A. Coupled Computational Fluid Dynamics-Discrete Element Method (CFD-DEM) Modeling of Moisture Removal in a Fluidized Bed Dryer for Heterogeneously Coated Solids. *Chem. Eng. Sci.* **2025**, *316*, 121811. [CrossRef]
27. Kim, Y.-S.; Lee, S.-D.; Baek, S.-M.; Baek, S.-Y.; Jeon, H.-H.; Lee, J.-H.; Abu Ayub Siddique, M.; Kim, Y.-J.; Kim, W.-S.; Sim, T.; et al. Development of DEM-MBD Coupling Model for Draft Force Prediction of Agricultural Tractor with Plowing Depth. *Comput. Electron. Agric.* **2022**, *202*, 107405. [CrossRef]
28. Su, J.; Zhou, C.; Jiang, X.; Qiao, Z. Orderly Arrangement of Agricultural Biomass Particles in Designed Gas–Solid Fluidized Beds Using CFD-DEM and Image Experiment. *Comput. Electron. Agric.* **2023**, *204*, 107510. [CrossRef]
29. Widartiningsih, P.M.; Mori, Y.; Takabatake, K.; Wu, C.-Y.; Yokoi, K.; Yamaguchi, A.; Sakai, M. Coarse graining DEM Simulations of a Powder Die-Filling System. *Powder Technol.* **2020**, *371*, 83–95. [CrossRef]
30. Shi, H.; Zhao, C.; Du, B.; Shen, G.; Ren, H. Calibration of Discrete Element Parameters and FEM-DEM Coupling Analysis for Solid Granules Medium Deep Drawing Forming. *Powder Technol.* **2025**, *463*, 121129. [CrossRef]
31. Chen, Z.; Ni, P.; Cheng, C.; Jia, P.; Hu, D.; Wu, M. Monitoring Interaction of Shallowly Buried, Large-Section, and Long-Distance Twin Box Jacking Tunnels with Small Spacing Under the Beijing-Hangzhou Grand Canal. *Tunn. Undergr. Space Technol.* **2024**, *153*, 105973. [CrossRef]
32. Lei, H.; Liu, Y.; Zhang, Y.; Hu, Y. Ground Deformation Behaviour Induced by Overlapped Shield Tunnelling Considering Vibration Loads of Subway Train in Sand. *Acta Geotech.* **2022**, *18*, 519–533. [CrossRef]
33. Wu, F.; He, C.; Kou, H.; Wang, B.; Meng, W.; Meng, H.; Guo, D. Discussion on Reasonable Clear Spacing of Twin-Tunnels in Weak Surrounding Rock: Analytical Solution and Numerical Analysis. *KSCE J. Civ. Eng.* **2022**, *26*, 2428–2442. [CrossRef]

Disclaimer/Publisher's Note: The statements, opinions and data contained in all publications are solely those of the individual author(s) and contributor(s) and not of MDPI and/or the editor(s). MDPI and/or the editor(s) disclaim responsibility for any injury to people or property resulting from any ideas, methods, instructions or products referred to in the content.